

2008

Plasma-Neutral Heat Transfer in Coaxial RF Argon Discharges

William B. Stein
Purdue University

Alina A. Alexeenko
Purdue University - Main Campus, alexeenk@purdue.edu

Ivana Hrbud
Purdue University

Follow this and additional works at: <http://docs.lib.purdue.edu/aaepubs>

 Part of the [Engineering Commons](#)

Recommended Citation

Stein, William B.; Alexeenko, Alina A.; and Hrbud, Ivana, "Plasma-Neutral Heat Transfer in Coaxial RF Argon Discharges" (2008).
School of Aeronautics and Astronautics Faculty Publications. Paper 33.
<http://dx.doi.org/10.2514/6.2008-5192>

This document has been made available through Purdue e-Pubs, a service of the Purdue University Libraries. Please contact epubs@purdue.edu for additional information.

Plasma-Neutral Heat Transfer in Coaxial RF Argon Discharges

William B. Stein*, Alina A. Alexeenko†, and Ivana Hrbud‡

Purdue University, West Lafayette, IN 47907, U.S.A.

Particle-in-cell/Monte Carlo Collision (PIC/MCC) algorithms comprise a numerical model to assess the discharge characteristics of an RF plasma microthruster concept that exploits an RF capacitively coupled discharge (RFCCD) to heat a propellant. The effects of heat transfer between the discharge and the neutral species on microthruster performance are discussed. Heat transfer within the plasma discharge has been shown to greatly affect the discharge characteristics and thruster performance. Increasing the neutral temperature reduces the amount of power transmitted into the fluid through a reduction of the neutral density, and thus reduces effectiveness of the discharge. The PIC/MCC modeling showed that the power transmitted into the fluid increases faster than linear with respect to an increase in applied potential, but the total power absorbed increases on the order of a linear trend. The power transmission efficiency is found to be directly proportional to the applied potential, making the discharge more efficient at higher voltages. The theoretical specific impulse also increases as the applied potential or discharge pressure is increased.

Nomenclature

\bar{T}_{gas}	Volume Averaged Neutral Temperature	K
\bar{u}, \vec{v}	Fluid Velocity	ms^{-1}
Δr	Length-step	m
Δt	Time-step	s
\dot{q}	Heat Flux	Wm^{-2}
ϵ	Permittivity	$CV^{-1}m^{-1}$
η_{PC}	Power Transmission Efficiency	$[\]$
Γ_{conv}	Convective Particle Loss Rate	m^3s^{-1}
$\Gamma_{electrode}$	Electrode Particle Diffusion Rate	m^3s^{-1}
Γ_e	Net Particle Generation Rate, Electron	m^3s^{-1}
Γ_{ion}	Ionization Rate	m^3s^{-1}
Γ_{recomb}	Recombination Rate	m^3s^{-1}
$\hat{r}, \hat{\phi}, \hat{z}$	Radial, Azimuthal, and Axial Directions	$[\]$
λ_{DE}	Debye Length	m
\mathbb{P}_C^{cx}	Power Loss to Charge Exchange Collisions	W
\mathbb{P}_C^{el}	Power Loss to Elastic Collisions	W
\mathbb{P}_C^{ex}	Power Loss to Excitation Collisions	W
\mathbb{P}_C^{in}	Power Loss to Ionization Collisions	W
\mathbb{P}_f	Power Transmitted into the Fluid	W
\mathbb{P}_W	Power Loss to Walls	W
\mathbb{P}_{abs}	Absorbed Power	W
\mathbb{P}_{in}	Input Power	W

*Ph.D. Candidate, E-mail: steinw@purdue.edu, AIAA Student Member.

†Assistant Professor, E-mail: alexeenk@purdue.edu, AIAA Member

‡Assistant Professor, E-mail: ihrbud@purdue.edu, AIAA Member

Copyright © 2008 by the American Institute of Aeronautics and Astronautics, Inc. The U.S. Government has a royalty-free license to exercise all rights under the copyright claimed herein for Governmental purposes. All other rights are reserved by the copyright owner.

ν_m	Electron-Neutral Collision Frequency	Hz
ν_{ex}	Excitation Collision Frequency	Hz
ν_{iz}	Ionization Collision Frequency	Hz
ν_{ng}	Neutral Gas Collision Frequency	Hz
ω	Angular Applied RF Frequency	Hz
ω_p	Plasma Frequency	Hz
ϕ	Applied Potential	V
ρ	Space Charge Density	Cm^{-3}
σ_0	Surface Charge on the Inner Electrode	Cm^{-2}
σ_1	Surface Charge on the Outer Electrode	Cm^{-2}
σ_{cx}	Ionization Cross-Section	m^{-2}
σ_{ele}	Elastic Cross-Section, Electron	m^{-2}
σ_{eli}	Elastic Cross-Section, Ion	m^{-2}
σ_{ex}	Excitation Cross-Section	m^{-2}
σ_{iz}	Ionization Cross-Section	m^{-2}
ε_e	Electron Energy	eV
ε_i	Ion Energy	eV
ε_{cx}	Energy Lost due to Charge Exchange	eV
ε_{el}	Energy Lost due to Elastic Collision	eV
ε_{ex}	Excitation Energy	eV
ε_{iz}	Ionization Energy	eV
\vec{B}	Magnetic Field	T
\vec{E}	Electric Field	Vm^{-1}
A_0	Inner Electrode Surface Area	m^2
A_1	Outer Electrode Surface Area	m^2
C_{plasma}	Capacitance of Plasma	F
d_{gap}	Gap Length of Discharge	m
e	Electron Charge	C
I_{spc}	Specific Impulse, Cold Gas Expansion	s
I_{sp}	Specific Impulse	s
j, \vec{J}	Current Density	Am^{-2}
k	Thermal Conductivity	$Wm^{-1}K^{-1}$
m	Neutral Particle Mass	kg
n_e	Electron Number Density	m^{-3}
n_g	Neutral Gas Number Density	m^{-3}
n_i	Ion Number Density	m^{-3}
nc	Number of Computational Cells	[]
$nc2p$	Ratio of Physical Particles to Computational Particles	[]
P	Pressure	Torr
$P_{collision}$	Collision Probability	[]
q	Charge	C
R_n	Uniform Random Number	[]
T	Temperature	K
T_e	Electron Temperature	eV

I. Motivation

Since the mid-90s, microsattellites (mass less than 100 kg) have been identified as an enabling concept for various future industry, military and science space missions. Microsattellites offer considerable value and effectiveness over a wide range of applications. Low complexity, manageable development, availability and applicability of low-cost technologies, low mass, low launch costs and non-conventional launch alternatives (piggy-back options) are attractive factors for many application needs. Besides the traditional demands by industry, academia, government and military agencies, developing countries around the world have deployed and are considering microsattellites as significant tools for disaster warning and farming, among others, due to their attractive attributes. To date, close to 100 small satellites (s/c mass below 250 kg) have been launched

into orbit. Notably, there has been a fast growth in the number of nanosatellites (mass of 20 kg and less) launched per year in the last decade.¹ These spacecraft are launched into orbits above 400 km with various inclinations to fulfill the specific need of the mission objective. The majority of these satellites possess no propulsion capability, while some are equipped with thrusters for initial orbit insertion such as cold gas microthrusters (SNAP-1),² chemical thrusters (XSS-10), micro pulsed plasma thrusters (FalconSat-3),³ and Hall thrusters (TacSat-2).⁴ An example of an industrial microsatellites program is ORBCOMM, one of very few fully deployed microsatellite constellation platforms that have 29 satellites in LEO, each equipped with a cold gas thruster for initial orbit insertion, but without any fuel allocation for stationkeeping.⁵ With the upcoming launch of the LISA Pathfinder Mission in 2009, micro-Newton colloidal thrusters will be tested on orbit as a part of the disturbance reduction system (ST7-DRS).⁶ ST7-DRS is a technology demonstration mission sponsored by NASA's New Millennium Program, which initiated research and development of advanced technologies for spacecraft. One of its major aspects is miniaturization to support high launch frequency of small, low-cost spacecraft. To date, this program spun off many micropropulsion system developments of both chemical and electric propulsion technologies. A prospective micropropulsion concept relies on a capacitive RF discharge between co-axial electrodes. The present paper explores numerical methods to assess propulsive capabilities of this concept as a potential micropropulsion system.

An alternative micropropulsion concept is the Radio-Frequency Capacitively Coupled Discharge (RFCCD) microthruster. This type of thruster is classified as an electrothermal system and has potential to overcome these severe microsatellite constraints. A capacitively coupled RF discharge between coaxial electrodes provides propellant heating and thermodynamic expansion of the gas generates thrust.

II. Background

A Radio-Frequency Capacitively Coupled Discharge is a type of gas discharge created by oscillating an applied potential across two electrodes at RF frequencies. The RFCCD is time variant, operates using both displacement and conduction currents and consists of two major regions. The discharge is composed of a central quasi-neutral region which is analogous to the positive column of a DC glow discharge and sheath regions which exist between the quasi-neutral core and each electrode. The sizes of each region depend on the operating pressure, applied voltage, and electrode sizes.⁷ The creation of sheaths represents a change in electron/ion number density due to electron/ion diffusion into the electrode itself and whose structure oscillates with the applied field. The energy of the applied electric field in RF discharge is being transferred to the bulk gas due to collisions between plasma species and the neutral propellant. The resulting plasma heating of the propellant can be exploited for electrothermal propulsion.

While this thruster technology is relatively new, RF discharges have been previously utilized as a propulsion mechanism, albeit in different ways.⁸⁻¹³ RF has been used as either a means for ion production in electrostatic thrusters, or a means to heat a fluid similarly to a microwave thruster operating a much lower frequency. RFCCD utilizes the RF component to contain as well as heat the ions produced by the glow discharge. The RFCCD has been investigated most extensively in the application to etching and sputtering.^{14,15} Etching/sputtering research is primarily devoted to a low-pressure discharge in argon with a goal to effectively sputter or etch the target material and not necessarily with a goal of heating the fluid. While the process is effectively the same, the objectives of a sputtering/etching discharge is the opposite of those required for an RF plasma thruster operation. Work has also been done regarding the use of different gases within the discharge.¹⁶⁻¹⁸ These investigations illustrate differences and possible benefits of utilizing different propellants for the RFCCD microthruster.

The most technically similar work was performed in 1999^{19,20} and focused primarily on investigating electrode erosion and the effect of characteristic operating parameters such as massflow, applied frequency, applied power, and electrode separation distance. It was performed with a large "proof-of-concept" thruster having an inner electrode diameter of approximately 5 cm. This work illustrated a reduction in electrode erosion when compared to operation in a DC mode as well as a small rise in temperature within the thruster.

Our previous work²¹⁻²³ investigated the effects of pressure and frequency on performance of a 50W RFCCD microthruster. This was done at a constant applied potential and inner radius corresponding to conditions similar to that in the experiments.²⁴ One selected favorable discharge case (3 Torr, 500 V, 200 MHz) and the corresponding plasma densities and gas heating formed the basis for an in-depth flow field and thrust performance analysis using the DSMC method. Assuming adiabatic wall conditions, the RF plasma thruster achieved a specific impulse of 63.8 s with argon at a throat Reynolds number of about 25. The

RF heating increases the specific impulse by 44% compared to cold gas thruster at the same geometry and pressure.

The present work discusses the effects of gas heat transfer within an RFCCD and their implications on microthruster performance. This is done by comparing the neutral gas temperature and the power transmitted into the fluid at various conditions. Trends of these variables are also explored as a function of applied potential and discharge pressure as well as their implications on theoretical specific impulse and power transmission efficiency.

III. Particle-In-Cell/Monte Carlo Collision Method

The Particle-In-Cell/Monte Carlo Collision (PIC/MCC) method is currently the most powerful approach for kinetic plasma modeling in the sub-continuum regime.^{25,26} PIC/MCC simulations are used in this model to determine plasma characteristics within the coaxial discharge chamber. The model used in this investigation utilizes *XPDC1*, a one-dimensional, bounded, cylindrical plasma simulation code developed by the Plasma Theory and Simulation Group at the University of California at Berkeley. *XPDC1* uses both particle-in-cell and Monte Carlo collision methods outlined by Birdsall²⁷ to simulate bounded plasma discharges. The simulation consists of a discharge region confined by coaxially arranged inner^a and outer electrodes of a finite length which are connected to an external circuit. The discharge consists of two species of particles, electrons and ions, suspended in a uniform background of neutral particles which are at a constant temperature. Both electrons and ions are discretized into computational *superparticles*, and represent a prescribed number of physical particles. These computational particles are initially distributed uniformly throughout the discharge and used to model collisional processes within the discharge. The charged particle dynamics are governed by their equations of motion. For nonmagnetized plasmas, a particle's equation of motion can be expressed as

$$m \frac{d\vec{v}}{dt} = q\vec{E} \quad (1)$$

A force is applied to a charged particle via an electric field, which determines the particle properties (\vec{r}, \vec{v}) within the discharge. Particle weighting is then applied to discretize these properties such that they can be applied to grid points determined by the cell boundaries. This allows for the particle properties to be numerically integrated along with the entire system. Weighting provides an efficient translation between the particles themselves and the properties developed at each cell boundary.

The boundary conditions of the discharge are determined using a potential applied across the electrodes from a voltage source^b and an external circuit. Applying Gauss' law to the system determines the boundary conditions of the discharge²⁷

$$\int_S \vec{E} \cdot d\vec{S} = \int_V \frac{\rho}{\epsilon} + \frac{A_0\sigma_0 + A_1\sigma_1}{\epsilon} = 0 \quad (2)$$

where the surface, S encloses the discharge and the electrodes. The areas A_0 and A_1 represent the inner and outer electrode areas and σ_0 and σ_1 represent the surface charge present on the inner and outer electrodes. ρ is the net space charge calculated from a sum of the electrons and ions within the discharge. This relationship can be discretized about each node of the grid using²⁷

$$r_{j+1/2}\Phi_{j+1} - 2r_j\Phi_j + r_{j-1/2}\Phi_{j-1} = \frac{-r_j\Delta r^2}{\epsilon}\rho_j \quad (3)$$

which is obtained by applying a central difference to Equation 2. At the outer electrode, the boundary condition $\Phi_b = 0$ is applied such that it is fixed at a reference potential while the boundary condition at the inner electrode is $E_a = \frac{\sigma_a}{\epsilon}$ and can be again rewritten using central difference as

$$E_{1/2} = \frac{\Phi_0 - \Phi_1}{\Delta_r} = \frac{1}{\epsilon} \left(\sigma_0 \frac{r_0}{r_{1/2}} + \frac{\rho_0}{2} \left[r_{1/2} - \frac{r_0^2}{r_{1/2}} \right] \right) \quad (4)$$

and is solved in a tridiagonal form at each timestep. Equation 4 is coupled to the external circuit using charge conservation at each electrode

$$A\Delta\sigma = Q_{conv} + \Delta Q \quad (5)$$

^aIt is possible to model a discharge without an inner electrode.

^bor a charge is applied to each electrode via a current source

where Q_{conv} represents the convective deposit of charge from the discharge and ΔQ represents the change in charge due to the external circuit. The charge on each electrode is advanced using Kirchoff's Voltage Law for a RLC circuit

$$L \frac{d^2 Q}{dt^2} + R \frac{dQ}{dt} + \frac{Q}{C} = V(t) + \Phi_1 - \Phi_0 \quad (6)$$

This is again discretized and solved along with Gauss' Law to form a self-consistent solution. To specify a capacitively coupled discharge, the capacitance of the external circuit is set to $1 F$, which is much greater than the capacitance of the plasma, $C \gg C_{plasma}$. This is done to ensure the majority of the voltage is applied across the discharge and not the blocking capacitor. The external circuit resistance and inductance are set to zero.

The argon collisional model employed in *XPDC1* includes electron-neutral ionization, lumped excitation and electron-neutral elastic scattering collisions using Lawler-Kortshagen cross-sections.²⁸ Ion-neutral resonant charge exchange and ion-neutral elastic scattering collisions are also incorporated.²⁹ The Lawler-Kortshagen cross-sections and the ion-neutral cross-sections are expressed as Equations 7-12

$$\sigma_{iz} = 3.18 \times 10^{-20} \ln \frac{\varepsilon_e}{\varepsilon_{iz}} \left(\frac{\varepsilon_e}{\varepsilon_{iz}} \right)^{-1} \quad \frac{\varepsilon_e}{\varepsilon_{iz}} > 1 \quad (7)$$

$$\sigma_{ex} = 1.56 \times 10^{-20} \ln \frac{\varepsilon_e}{\varepsilon_{ex}} \left(\frac{\varepsilon_e}{\varepsilon_{ex}} \right)^{-1} \quad \frac{\varepsilon_e}{\varepsilon_{ex}} > 1 \quad (8)$$

$$\sigma_{el_e} = 1.59 \times 10^{-19} \frac{\varepsilon_e}{11.55} \quad \varepsilon_e \leq 11.55 eV \quad (9)$$

$$\sigma_{el_e} = 1.59 \times 10^{-19} \sqrt{\frac{\varepsilon_e}{11.55}} \quad \varepsilon_e > 11.55 eV \quad (10)$$

$$\sigma_{el_i} = (7.0 - 0.380 \ln \varepsilon_i)^2 \times 10^{-20} \quad (11)$$

$$\sigma_{cx} = (6.45 - 0.365 \ln \varepsilon_i)^2 \times 10^{-20} \quad (12)$$

where $\varepsilon_{iz} = 15.76$ eV and $\varepsilon_{ex} = 11.62$ eV for argon. The particle energy determines the cross-section for each type of collision. These properties along with properties of the neutral species determine the collisional probability for the m^{th} particle in a time-step Δt as

$$P_{collision,m} = 1 - e^{-n_g \sigma(\varepsilon_m) \nu_m \Delta t} \quad (13)$$

The collisional probability is then compared to a uniform random number, R_n . If $P_{collision,m} > R_n$, the particle collides and is scattered in the time-step Δt . The type of collision is determined and the appropriate scattering angle and velocity change. If ionization and excitation collisions occur, an energy balance is performed on the system of particles to determine their new velocities, including the internal energy loss. For a given number of particles per cell, with a cell-collisional cross-section (determined by the particles with the maximum energy), $P_{collision,m} \times n_p$ particles may collide, and each of these particles are then checked to determine its collisional state. The entire PIC/MCC process is shown in Figure 1. The computational parameters of the PIC model were chosen to meet the following criteria for numerical accuracy:

- Number of Cells: $nc \geq \frac{2d_{gap}}{\lambda_D}$
- Time-step: $\Delta t \leq \frac{0.2}{\omega_p}$ -and- $\Delta t \leq \frac{1}{\omega}$
- Ratio of Computational to Physical Particles: Determined such that $nc2p$ results in ≈ 50 -100 computational particles per cell at steady state

The discharge is simulated for at least 1000 RF cycles until the plasma number densities stabilize within $\pm 1\%$ of the average number density of the last 100k timesteps.

The estimated statistical errors for the various power loss mechanisms are shown in Table 1 and are calculated by taking the ratio of the standard deviation to its average. The values in Table 1 represent averages of the statistical errors for all the cases simulated at the specified conditions. The average statistical error in both the electron and ion number densities for all conditions was less than 1% and is not shown.

The power lost to the walls presents the largest statistical error for these cases, with the power lost to ionization collisions being the next largest. These errors can introduce large uncertainties in the calculation

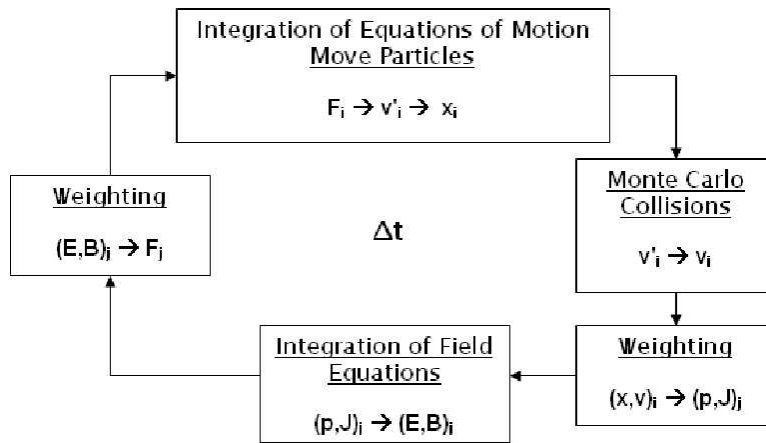


Figure 1. Flowchart of PIC Algorithm

Table 1. Comparison of Estimated Statistical Errors for the Different Power Loss Mechanisms

Conditions:		% P_C^{in}	% P_C^{cx}	% P_C^{ex}	% P_f	% P_W
1 mm	100 V	10	6	5	5	23
5 mm	100 V	18	10	7	9	47
1 mm	500 V	18	10	9	10	48
5 mm	500 V	25	14	10	14	79
3 Torr	200 MHz	28	6	6	6	60

of the power transmission efficiency, especially when the power transmission efficiency is small. For regions where the power transmission efficiency is relatively high for instance, the 5 mm inner radius 500 V cases, the magnitude of the power lost to ionization and the walls is relatively small when compared to that of the power transmitted into the fluid or the power lost to excitation. This is mainly because the power transmitted into the fluid and the power lost to excitation collisions represent the majority of the power absorption in the discharge. Thus, as power transmission into the fluid increases, the overall effect of these statistical errors on the power transmission efficiency is reduced.

IV. Neutral Temperature Model

Since the main goal of these simulations is to study the performance and behavior of a microthruster which utilizes an RFCCD to heat a working fluid, neutral gas heating effects need to be taken into consideration. *XPDC1* was originally written to model different plasma discharges at lower pressures where modeling via PIC simulations is efficient. Within this realm, heat transfer to the neutral gas species can be considered negligible and thus is not simulated. This investigation borders on the periphery of this model and must range from a collisionless regime to that of a continuum, where changes in neutral gas temperature become more prevalent. Thus, gas temperature variation must be incorporated in order to make the simulation self-consistent within sub-continuum and continuum regimes. Both the original constant temperature and gas heat transfer models were used in order to better understand the effect of heat transfer within the discharge.

The original code, *XPDC1*, was augmented to incorporate real-time changes in the discharge as a result of plasma heating. The neutral gas temperature is calculated based on period-averaged power transmission into the fluid by solving 1-D heat conduction in the coaxial electrode gap with fixed temperature boundary conditions. This is traditionally solved using Joule heating with a diffusion-drift approximation.³⁰ In PIC simulations though, it is possible to utilize the actual power transmission that occurs with the various types of plasma-neutral collisions.

$$-\frac{1}{r} \frac{\partial}{\partial r} \left[rk \frac{\partial T}{\partial r} \right] = \langle P_f \rangle \quad (14)$$

Four power loss mechanisms exist in this regime, namely due to elastic P_C^{el} , charge exchange P_C^{cx} , ionization P_C^{iz} , and excitation collisions P_C^{ex} . The power transmitted into the fluid consists only of the first two power

loss mechanisms. These power loss mechanisms are calculated for both species using the following relations:

$$\text{Wall Diffusion:} \quad \mathbb{P}_W = \frac{e \, nc2p \, \varepsilon_e}{\Delta t} \quad (15)$$

$$\text{Ionization:} \quad \mathbb{P}_C^{iz} = \frac{e \, nc2p \, \varepsilon_{iz} \nu_{iz}}{\Delta t} \quad (16)$$

$$\text{Excitation:} \quad \mathbb{P}_C^{ex} = \frac{e \, nc2p \, \varepsilon_{ex} \nu_{ex}}{\Delta t} \quad (17)$$

$$\text{Elastic Collisions:} \quad \mathbb{P}_C^{el} = \frac{e \, nc2p \, \varepsilon_{el}}{\Delta t} \quad (18)$$

$$\text{Charge Exchange Collisions:} \quad \mathbb{P}_C^{cx} = \frac{e \, nc2p \, \varepsilon_{cx}}{\Delta t} \quad (19)$$

$$\text{Transmitted into the Fluid:} \quad \mathbb{P}_f = \mathbb{P}_C^{cx} + \mathbb{P}_C^{el} \quad (20)$$

Due to the assumption that Coulomb collisions are negligible, there are only certain combinations of collisions that are modeled in this simulation. Electrons can collide with neutrals via elastic, ionization, or excitation collisions whereas ions and neutrals collide elastically or via charge-exchange. Elastic and charge-exchange collisions directly transfer energy from the plasma to the neutrals. Conversely, ionization and excitation collisions serve a different purpose. Ionization collisions create ion-electron pairs which help sustain the plasma and offset diffusion losses. The remaining energy that is not used to ionize the neutral atom is transferred directly to the energy of the new ion/electron pair. The power lost to excitation collisions is regarded as a similar loss mechanism. It is not used to heat the working fluid, but is lost via the excitation of electrons within the outer valence shells of the neutral molecules which is then re-emitted via the “glow”. While it is understood that some of the photonic power re-emitted from the excited neutrals could be used to heat the fluid, it is believed to be negligible in comparison to the sum of the other heating mechanisms and is not modeled in this simulation.

The neutral gas temperature is calculated using Gaussian elimination with partial pivoting every 1,000 time steps. A distribution of the time-averaged power transmitted into the fluid is used to solve for the temperature distribution throughout the discharge. The thermal conductivity of argon is calculated using a power-law temperature model and the temperature distribution at the previous timestep

$$k = \frac{3}{2} C_p \mu_{ref} \left(\frac{T}{T_{ref}} \right)^{\omega_v} \quad (21)$$

with $\mu_{ref} = 2.117 \times 10^{-5} \, Nm^{-2}s$, $C_p = 524 \, Jkg^{-1}K^{-1}$, $T_{ref} = 273.2 \, K$, and $\omega_v = .81$. The temperature boundary conditions for this investigation have been set to 300 K since the wall thermal boundary conditions are dependent on the specific thruster design and operating conditions than a specific value.

The neutral gas temperature within the discharge is solved using Gaussian elimination with partial pivoting for discretized numerical derivatives of Fourier’s Conduction Equation:

$$\frac{1}{r} \frac{\partial}{\partial r} \left(kr \frac{\partial T}{\partial r} \right) + \dot{q} = 0 \quad (22)$$

While $k = f(T)$, it is assumed constant at each timestep and thus can be removed from the derivative. When numerically solving for the temperature k becomes solely a function of radius, and is calculated using values from the previous timestep. Using the central difference method Equation 22 becomes

$$-\frac{1}{2} \left\{ 1 + \frac{dr}{2r_i} \right\} T_{i+1} + T_i - \frac{1}{2} \left\{ 1 - \frac{dr}{2r_i} \right\} T_{i-1} = \frac{\dot{q} dr^2}{2k_1} \quad (23)$$

and can be solved using Gaussian elimination with partial pivoting to determine the temperature distribution within the discharge. The temperature solver was compared to analytical solutions which were solved using constant thermal conductivities. The appropriate heat-source terms were back-calculated from desired temperature distributions and then inserted into the numerical model to compare the numerically solved temperature distribution to that of the chosen analytical solution. This procedure was performed for many different temperature distributions to observe the validity of the model under different conditions, all of which produced similar results. The thermal conductivity model was also validated separately using three different sets of experimental data. The thermal conductivity model was derived using the method presented in Bird Eq.3.56 and using a variable hard sphere model (VHS).³¹

V. Discharge Properties

The electron and ion motions within the gas discharge are governed by the applied electric potential and momentum transfer due to collisions with neutral gas molecules.¹⁵ Coulomb collisions between ions and electrons can be neglected for an RF discharge of this type due to weak ionization, typically $n_i/n_g < 10^{-3}$. The oscillations of ions and electrons in a gas discharge are due to a combined effect of two processes, namely the drift of charges in an electric field and momentum transfer due to collisions. The frequency of such oscillations depends on the effective collision frequency of momentum transfer between charged particles and gas neutrals ν_m , and the applied frequency ω . The ratio between the two frequencies is thus a non-dimensional number that characterizes the collisional regime. In a limiting case, when $\omega/\nu_m \ll 1$, the plasma is described as a collisional continuum governed by the electrohydrodynamic equations. Conversely, for $\omega/\nu_m \gg 1$, the ions and electrons undergo free oscillations in a collisionless manner which is described by ballistic-type models. In the transitional regime between the continuum and collisionless plasmas, a kinetic description based on the distribution function of charges is required. For argon, the effective frequency of momentum transfer due to plasma collisions is estimated as^{32,33}

$$\nu_m = \nu_{m0} P \left(\frac{T_{ref}}{T} \right) \quad (24)$$

with pressure in Torr and $\nu_{m0} = 5.3 \times 10^9 \frac{\text{Hz}}{\text{Torr}}$ for argon. Figure 2 shows the collisional regimes of argon discharge as a function of gas pressure and applied frequency. For pressures larger than 10 Torr, the plasma lends itself to a continuum description for frequencies up to 1 GHz. For pressures below 10 Torr, the discharge is in a non-continuum regime for the whole RF frequency range. Therefore, to accurately predict argon discharge characteristics at low and moderate pressures, this study applies a kinetic approach based on particle-in-cell method with Monte Carlo collisions (PIC/MCC).

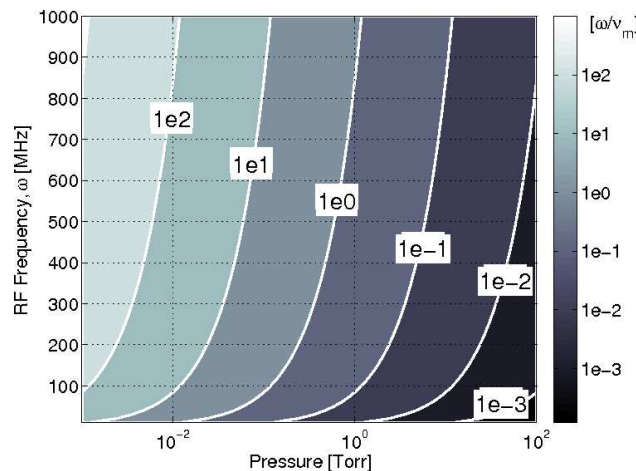


Figure 2. Collisional Regimes for Argon as a Function of Applied Frequency and Pressure at 300 K

RFCCD microthruster performance is characterized chiefly by its ability to efficiently convert energy of the applied electric field into the propellant enthalpy and then to kinetic energy in the nozzle expansion. This ability can be characterized through a ratio of power transmission into the fluid over the total absorbed power

$$\eta_{PC} = \frac{P_f}{P_f + P_C^{ex} + P_C^{in} + P_w} \quad (25)$$

This parameter η_{PC} is an indicator of how much power is available to heat the fluid for a given amount of total power delivered to the thruster. Increasing the power transmitted into the fluid increases the neutral temperature and thus improves microthruster performance. This can also provide a metric for evaluating electrode erosion. While particle collisions with the electrodes cannot be totally eliminated in general, conditions can be sought that effectively minimizes the power lost to the electrodes.

This analysis also considers limitations in applied power. The PIC/MCC code incorporates either a voltage-limited or current-limited source but does not include any type of power limitation. This poses a problem since the applied power will be physically limited by the type of power supply that is ultimately

used. For the scope of this analysis, cases which have a total power absorption of approximately 50-75 W are considered desirable for a thruster of this type and mission. Other cases which provide a power consumption outside this range are presented to express overall trends, but are not used for thruster design.

For discharges operating at these conditions, ionization and particle diffusion dominate the net particle generation rates, whereas recombination and convective losses have been found to be negligible.^{30,34} These rates are compared for a design case in Table 2.

Table 2. Comparison of Net Particle Generation Rates for the Design Case: P=3 Torr, $\omega=200$ MHz, V=500 V, $R_0=5$ mm

Sample Data Averaged over 100 Points		
Ionization Events	6.62E8	[events]
Δt	2.46E-9	[s]
Particles Lost to Walls	6.42E8	[particles]
Electron Number Density	1.76E18	[m^{-3}]
Electron Temperature	≈ 4	[eV]
Neutral Drift Velocity	≈ 2	[ms^{-1}]
Discharge Gap Length	6.5	[mm]
Net Particle Generation Rate Characteristics		
Γ_{Ion}	0.15	[$m^3 s^{-1}$]
Γ_{Recomb}	9.55E-20	[$m^3 s^{-1}$]
Γ_{Conv}	1.75E-16	[$m^3 s^{-1}$]
$\Gamma_{Electrode}$	0.14	[$m^3 s^{-1}$]

VI. Plasma-Neutral Heat Transfer Effects

To better understand how gas heat transfer affects the characteristics of the plasma discharge and their performance implications on an RFCCD microthruster, four cases were analyzed with both temperature models. Each case corresponds to a different power level at a different set of input conditions and the results from this analysis are shown in Table 3.

Table 3. The Effects of Neutral Temperature on Discharge Characteristics

Conditions:				\bar{T}_{gas} [K]	\bar{n}_e [m^{-3}]	\mathbb{P}_f [W]	η_{PC}
3 Torr	200 MHz	3 mm	59 V	312.42	1.35e17	0.44	0.18
3 Torr	200 MHz	5 mm	500 V	605.87	1.12e18	30.22	0.68
10 Torr	1000 MHz	1 mm	100 V	430.42	5.90e18	6.26	0.33
1 Torr	600 MHz	1 mm	500 V	558.22	3.04e18	14.8	0.49

How the neutral gas heat transfer affects the discharge characteristics depends on the operating conditions of the thruster. Over this range of input conditions, the power transmitted into the fluid varies greatly. Even at a lower power, heat transfer to the neutrals is non-negligible. As power is transmitted to the neutral gas, the neutral temperature rises, reducing the gas density and thus the neutral collision frequency. This reduces the plasma's effectiveness to transmit power into the fluid and thus reduces the gas temperature until the discharge becomes stable. Thermal conductivity effects are also non-negligible, especially for higher power/higher temperature discharges. The temperature distributions for these four cases are compared in Figure 3.

Gas heat transfer not only affects the bulk parameters of the discharge but also affects the shape of the discharge as well. The presence of higher neutral temperatures in the discharge reduces the electron number densities of the plasma, as aforementioned, but also affects their distribution shape. An increase in neutral temperature effectively reduces the discharge pressure via a reduction in neutral number density. This effect can be shown using the plasma-neutral collision frequency estimated in Equation 24.

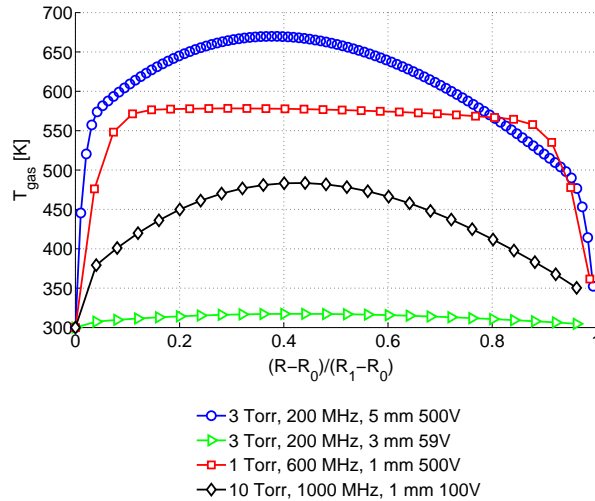


Figure 3. Comparison of Temperature Profiles, Gas Heat Transfer Model

Neutral temperature and power transmission effects were also explored. These cases were simulated using a 160 MHz applied frequency, a 3.175 mm inner radius, and at discharge pressures of 1.9, 3.5, and 5.0 Torr. Figure 4 illustrates both \mathbb{P}_{abs} and \mathbb{P}_f versus applied potential. Both types of power consumption increase as a function of pressure and voltage as expected from earlier studies.^{21,22} It is of note that the \mathbb{P}_f increases with applied potential much faster than \mathbb{P}_{abs} . The total absorbed power increases in a near linear fashion above potentials of approximately 75 V at which the discharges transition and will be discussed in more detail below.

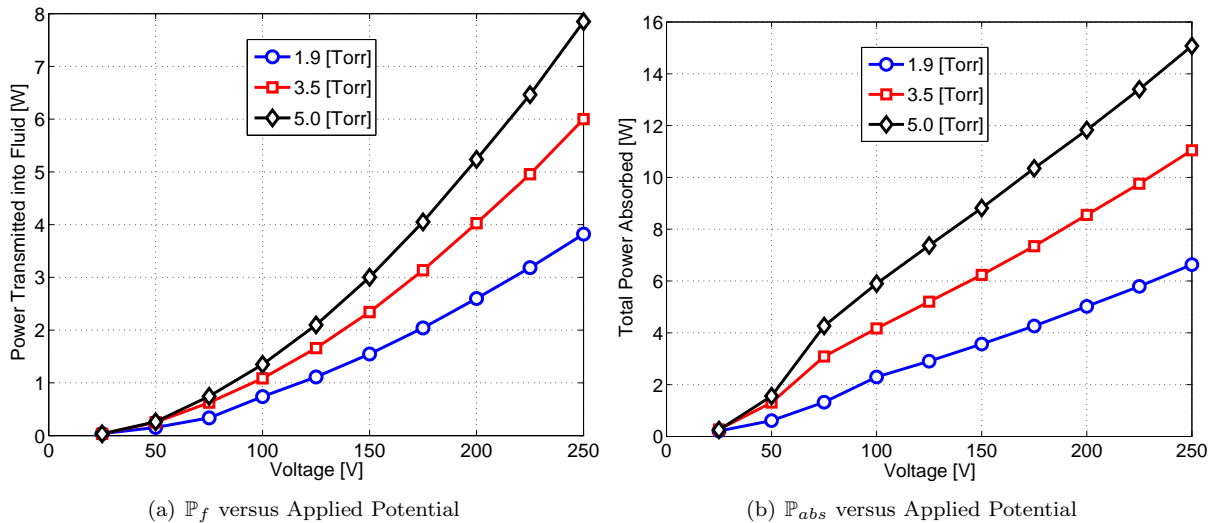
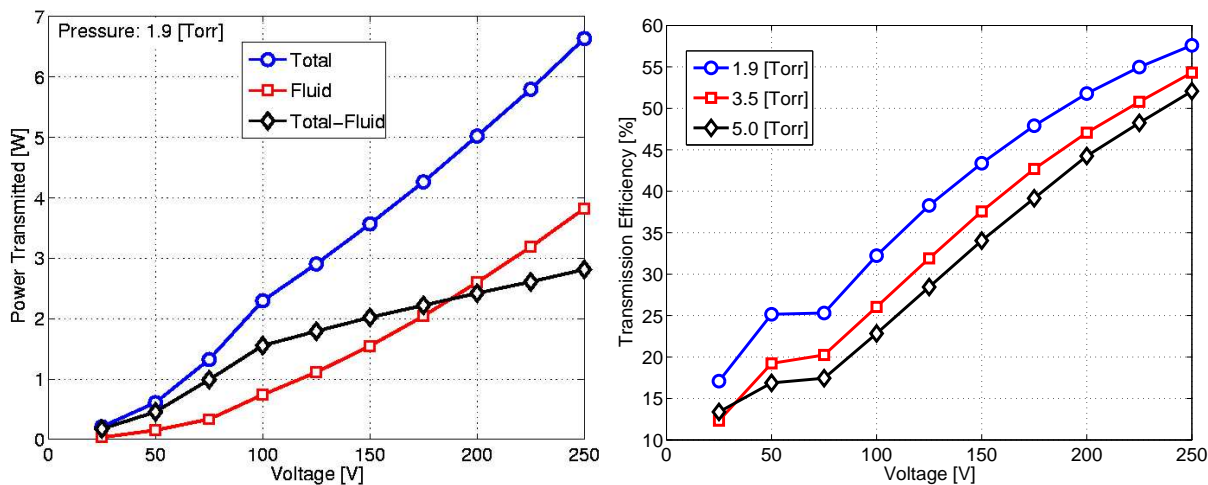


Figure 4. Power Consumption versus Applied Potential, 160 MHz, 3.175 mm

Figure 5(a) shows the power transmitted into the fluid, the total absorbed power, and the remaining power losses as a function of applied potential at a constant pressure of 1.9 Torr. While the power transmitted into the fluid increases at a faster rate than that of the total absorbed power, there are always other modes of power losses present. As the applied potential is increased, the power losses increase at a much slower rate than the power transmitted into the fluid. Thus, the discharge becomes more efficient as the applied potential is increased. The discharge becomes 50% efficient when the \mathbb{P}_f equals power loss and happens between 175 and 200 V at a discharge pressure of 1.9 Torr. This point is also shown in Figure 5(b).

The relationship between the transmission efficiency and the applied potential is shown in Figure 5(b). Again, the trend changes at the transition voltage, changing from a sharp increase in transmission efficiency

into one that increases slower than linear. The transmission efficiency increases quicker for lower pressures, but also approaches a maximum or asymptotic value quicker. Figure 5(b) also suggests that there may be a maximum transmission efficiency for which a discharge operating at a given set of conditions may attain, i.e. an increase in potential no longer increases the transmission efficiency as effectively.



(a) Comparison of Power Transmission and Losses at 1.9 Torr (b) Power Transmission Efficiency versus Applied Potential
Figure 5. Comparison of Power Transmission and Transmission Efficiency at 160 MHz, 3.175 mm

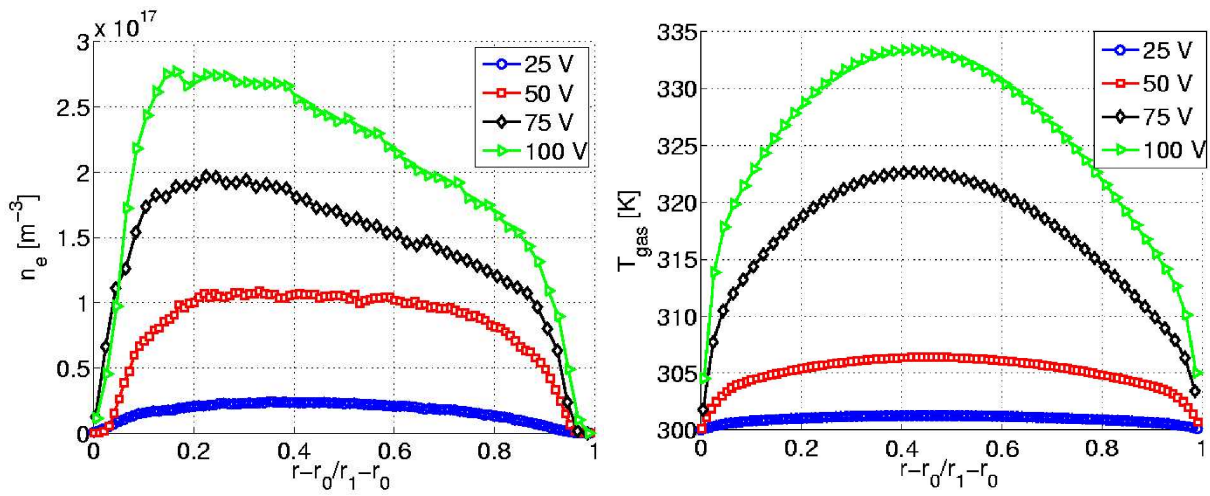
As previously mentioned, trends in Figures 4(b) and 5(b) change as the potential decreases below 75 V. Discharges below 75 V show a lower P_{abs} than would be predicted by the near-linear trend seen above 75 V, with very weak discharges (< 0.25 W) at 25 V. Also, there is little change in power transmission efficiency between 50 and 75 V. This transition region can be explained via changes in the plasmadynamics of the discharge. It is apparent from Figure 4(a) that this transition region does not appear in trends of P_f versus applied voltage. Thus, this transition must be solely a function of the excitation and ionization power losses as well as influenced by power losses to the electrodes. At the lower voltages (25, 50 V), there is enough ionization to sustain a discharge, but the discharge is still dominated by diffusion losses. Only until the applied potential increases past approximately 75 V does the discharge become fully developed. This transition from a diffusion dominated discharge to a more developed discharge is illustrated in Figure 6(a) with changes in temperature distributions in the discharges shown as Figure 6(b). Beyond this transitional region, the charge-exchange power loss outpaces both the excitation and ionization power losses, creating a more efficient discharge.

Figure 7(a) compares neutral temperature in the discharge to the applied potential. The neutral temperature increases slightly faster than linear, with two different slopes corresponding to either side of the transition potential and is only a weak function of discharge pressure. This is surprising given the fact that the power transmitted into the fluid can increase with an increase in discharge pressure. The effect on neutral temperature can also be expressed as a percent increase in the theoretical specific impulse relative to that derived from a cold gas expansion for a converging nozzle in continuum using:

$$\frac{I_{sp}}{I_{spc}} = \sqrt{\frac{T_0}{T_{ref}}} \quad (26)$$

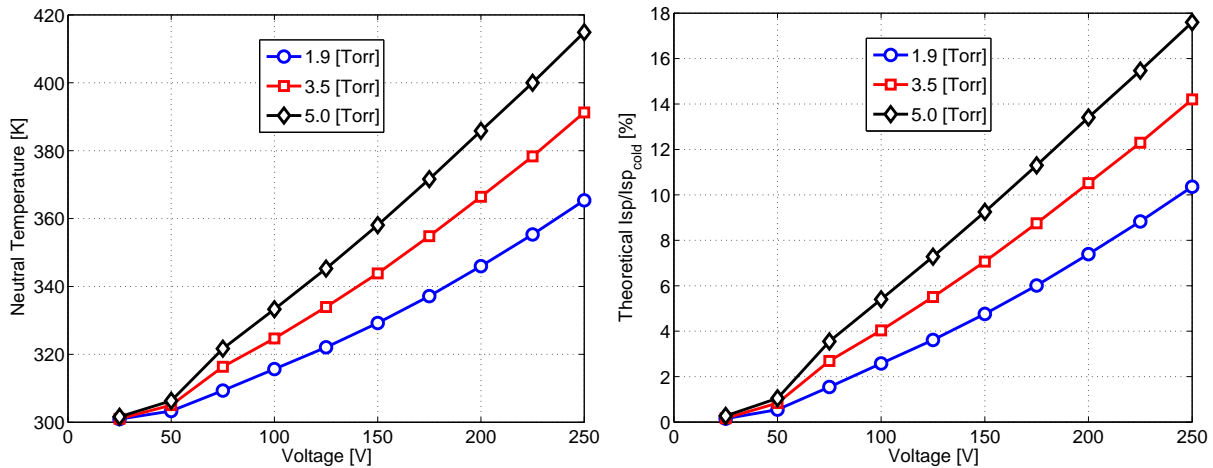
where T_{ref} is 300 K and the theoretical I_{sp} for a cold gas expansion is 56.8 s. The theoretical specific impulse is illustrated in Figure 7(b) and shows a trend similar to that of the neutral temperature in Figure 7(a). The theoretical I_{sp} increases in an approximately linear fashion with respect to applied potential and the discharge pressure above the transition potential.

The slopes of the theoretical I_{sp} versus pressure data are 0.34 and 1.33 for constant voltages of 75 and 250 V respectively, with the slopes of the theoretical I_{sp} versus voltage data being 0.03 and 0.05 for constant pressures of 1.9 and 5.0 Torr. Thus, an increase in the discharge pressure is more beneficial in terms of theoretical I_{sp} than an increase in applied potential.



(a) Electron Number Density Distribution Transition with an Increase in Applied Potential (b) Temperature Distribution Transition with an Increase in Applied Potential

Figure 6. Discharge Transition due to an Increase in Applied Potential



(a) Neutral Temperature versus Applied Potential

(b) Percent Increase in Theoretical Isp versus Applied Potential

Figure 7. Discharge Performance versus Applied Potential, 160 MHz, 3.175 mm

VII. Conclusions

An RFCCD discharge was successfully modeled using a PIC/MCC method. It has been demonstrated that there is a transition voltage below which discharges are diffusion dominated, yet sustainable. A gas heat transfer solver was implemented within PIC/MCC simulations and illustrated where heat transfer to the neutrals plays an integral part in determining discharge characteristics. The plasma-neutral collision frequency is the largest influencing factor for determining power transfer to the fluid. Thruster performance and discharge characteristics can be further improved by increasing the applied potential. Power transmission into the fluid and power transmission efficiency increases with an increase in applied potential which has also been demonstrated in previous studies.

Acknowledgments

The authors would like to thank Dr. J.P. Verboncoeur, Dr. C.K. Birdsall and the Berkeley Plasma Theory and Simulation Group for the use of their *XPDC1* code and providing assistance. We would also like

to thank Dr. Mikhail Shneider for extremely valuable discussions of RF discharge physics. The computations reported in this paper were performed on 16 CPU Sunfire 4600 awarded through Sun Microsystems, Inc. Academic Excellence Grant #EDUD-7824-070336-US.

References

- ¹Caceres, M., "The emerging nanosatellite market," *Aerospace America*, February 2001, pp. 16–18.
- ²Baker, A. and Underwood, C., "Micropropulsion from Snap to PALMSAT: When Does MEMS Become the Way Forward?" *Proceedings of NanoTech 2002 - "At the Edge of Revolution"*, AIAA-2002-5759, Houston, TX, Sept. 2002.
- ³White, D., Schilling, J. H., Bushman, S., Spanjers, G., Bromaghim, D., Lake, J., and Dulligan, M., "AFRL MicroPPT Development for Small Spacecraft Propulsion," *33rd Plasmadynamics and Lasers Conference, AIAA 2002-2120, Maui, HI*, May 2002.
- ⁴Reed, G. D. and Hargus, W. A., "Complementary Plasma Density Measurements for the BHT-200-X3 Hall Thruster Plume," *42nd AIAA Joint Propulsion Conference, AIAA 2006-4992, Sacramento, CA*, July 2006.
- ⁵Maclay, T. and Tuttle, C., "Satellite Stationkeeping Of The ORBCOMM Constellation Via Active Control Of Atmospheric Drag: Operations, Constraints, And Performance," *Advances in the Astronautical Sciences, Part I*, Vol. 120, 2005, pp. 763–773.
- ⁶Ziemer, J., Gamero-Casta, M., Hraby, V., Spence, D., Demmons, N., McCormick, R., Roy, T., Gasdaska, C., Young, J., and Connolly, B., "Colloid Micro-Newton Thruster Development for the ST7-DRS and LISA Missions," *41st AIAA Joint Propulsion Conference, AIAA-2005-4265, Tucson, Arizona*, July 2005.
- ⁷Alves, M., Lieberman, M., Vahedi, V., and Birdsall, C., "Sheath Voltage Ratio for Asymmetric RF Discharge," *Journal of Applied Physics*, Vol. 69, No. 7, 1991, pp. 3823–3829.
- ⁸Leiter, H. and Feili, D., "RIT 15S- A Radio Frequency Ion Engine for High Specific Impulse Operation," *37th AIAA Joint Propulsion Conference*, July 2001, AIAA Paper 2001-3491.
- ⁹Pollard, J., Lichtin, D., and Cohen, R., "RF Discharge Electrothermal Propulsion: Results from a Lab-Scale Thruster," *23rd AIAA Joint Propulsion Conference*, 1987, AIAA Paper 1987-2124.
- ¹⁰Groh, K. and H.W.Loeb, "State-of-the-Art of Radio Frequency Ion Thrusters," *Journal of Propulsion and Power*, Vol. 7, No. 4, 1991, pp. 573–579.
- ¹¹Brewer, L., Karras, T., and Graham, D., "Preliminary Results of a High Power RF Thruster Test," *25th AIAA Joint Propulsion Conference*, 1989, AIAA Paper 1989-2382.
- ¹²Olson, L., "Operation of a 50 W Radio Frequency Plasma Thruster," *37th AIAA Joint Propulsion Conference*, 2001, AIAA Paper 2001-3903.
- ¹³A, M. and Hushfar, F., "Radio Frequency Heating of a Dense Moving Plasma," *AIAA Electric Propulsion Conference*, March 1963, 63045-63.
- ¹⁴Raizer, Y., Shneider, M., and Yatsenko, N., *Radio Frequency Capacitive Discharges*, CRC Press, 1995.
- ¹⁵Lieberman, M. and Lichtenberg, A., *Principles of Plasma Discharges and Materials Processing, 2nd Edition*, John Wiley and Sons, 2005.
- ¹⁶Moravej, M., Yang, X., and Hicks, R., "A Radio-Frequency Nonequilibrium Atmospheric Pressure Plasma Operating with Argon and Oxygen," *Journal of Applied Physics*, Vol. 99, 2006, pp. 093305 1–6.
- ¹⁷Sommerer, T., Hitchon, W., and Lawler, J., "Electron Heating Mechanisms in Helium rf Glow Discharges: A Self-Consistent Kinetic Calculation," *Physical Review Letters*, Vol. 63, No. 21, 1989.
- ¹⁸Novikova, T., Kalache, B., and Bulkin, P., "Numerical Modeling of Capacitively Coupled Hydrogen Plasmas: Effects of Frequency and Pressure," *Journal of Applied Physics*, Vol. 93, No. 6, 2003, pp. 3198–3206.
- ¹⁹White, P. S., Best, S., Hrbud, I., Hartsfield, R., and Rose, M., "RF Plasma Thruster for SmallSat Applications," *35th AIAA Joint Propulsion Conference*, 1999, AIAA 1999-2438.
- ²⁰White, P., *Preliminary Investigation of an RF Plasma Thruster*, Master's thesis, Auburn University, 1999.
- ²¹Stein, W., Alexeenko, A., and Hrbud, I., "Performance Modeling of a Coaxial Radio-Frequency Gas Discharge Microthruster," *Journal of Propulsion and Power*, Accepted April 2008.
- ²²Stein, W., Alexeenko, A., and Hrbud, I., "RFCCD Microthruster Performance via Numerical Simulation," *AIAA Paper 2008-0962*, 2007.
- ²³Stein, W., Alexeenko, A., and Hrbud, I., "Performance Modeling of an RF Coaxial Plasma Thruster," *43rd AIAA Joint Propulsion Conference*, 2007, AIAA Paper 2007-5292.
- ²⁴Hrbud, I., Kemp, G. E., Yan, A. H., and Gedrimas, J. G., "Review of RF Plasma Thruster Development," *IEPC Paper 2007-309, 30th International Electric Propulsion Conference, Florence, Italy*, Sept. 2007.
- ²⁵Lawson, W., "Particle Simulation of Bounded 1D Plasma Systems," *Journal of Computational Physics*, Vol. 80, 1989, pp. 253–276.
- ²⁶Schweigert, I. and Schweigert, V., "Combined PIC-MCC Approach for Fast Simulation of a Radio-Frequency Discharge at a Low Gas Pressure," *Plasma Sources Science and Technology*, Vol. 13, 2004, pp. 315–320.
- ²⁷Birdsall, C., "Particle-in-Cell Charged-Particle Simulations Plus Monte Carlo Collisions With Neutral Atoms, PIC-MCC," *IEEE Transactions on Plasma Science*, Vol. 19, No. 2, April 1991, pp. 65–85.
- ²⁸Lawler, J. and Kortshagen, U., "Self-Consistent Monte Carlo Simulations of the Positive Column of Gas Discharges," *Physics D: Applied Physics*, Vol. 32, 1999, pp. 3188–3198.
- ²⁹*Cylindrical Plasma Device 1-D Bounded Electrostatic Code*, Plasma Theory and Simulation Group, University of California, Berkeley.
- ³⁰Raizer, Y. P. and Shneider, M., "Coaxial Medium-Pressure RF Discharge: Dynamics of Plasma Oscillations," *Plasma Physics Reports*, Vol. 21, 1995, pp. 260–267.

³¹Bird, G., *Molecular Gas Dynamics and the Direct Simulation of Gas Flows*, Oxford University Press, 2004.

³²Raizer, Y., *Gas Discharge Physics*, Springer-Verlag, 1991.

³³Fridman, A. and Kennedy, L., *Plasma Physics and Engineering*, Taylor & Francis Group, 2004.

³⁴Shneider, M., Zhang, Z., and Miles, R., "Plasma Induced by Resonance Enhanced Multiphoton Ionization in Inert Gas," *Journal of Applied Physics*, Vol. 102, 2007, pp. 123103 1–7.